AEROSOL SCIENCE AND TECHNOLOGY
2023, VOL. 57, NO. 4, 355–366
https://doi.org/10.1080/02786826.2023.2176739

Taylor & Francis
Taylor & Francis Group

TECHNICAL NOTE

Check for updates

High-accuracy effective density measurements of sodium methanesulfonate and aminium chloride nanoparticles using a particulate calibration standard

Véronique Perraud[a], James N. Smith[a], and Jason Olfert[b]

[a]Department of Chemistry, University of California, Irvine, California, USA; [b]Department of Mechanical Engineering, University of Alberta, Edmonton, Alberta, Canada

ABSTRACT

Methanesulfonate and aminium salts are commonly found in ambient nanoparticles and are often used as calibration standards. However, the effective densities of the particles generated from these standards are required if they are to be used to calibrate aerosol mass spectrometers or to estimate hygroscopic growth factors from electrodynamic balance experiments. A centrifugal particle mass analyzer and scanning mobility particle sizer were used in tandem (CPMA-SMPS) to measure the effective density of five salts. The effective densities were determined to be: sodium methanesulfonate, 1474 ± 13 kg m^{-3}; methylammonium chloride, 1236 ± 29 kg m^{-3}, monoethanolamine hydrochloride, 1136 ± 26 kg m^{-3}; 1,4-diaminobutane dihydrochloride, 1135 ± 33 kg m^{-3}; and NaCl was found to have a size-dependent effective density due to its non-spherical shape. It is also shown how Santovac® vacuum pump oil can be used to accurately calibrate the CPMA-SMPS system for particles less than 100 nm in diameter, which is a size range that has been problematic for calibration techniques relying on polystyrene latex spheres.

ARTICLE HISTORY
Received 2 August 2022
Accepted 27 January 2023

EDITOR
Jingkun Jiang

1. Introduction

Atmospheric particles are well known to impact climate (IPCC, 2021) and have deleterious effects on human health (Pope and Dockery 2006; Heal, Kumar, and Harrison 2012; Lelieveld et al. 2015; Lelieveld 2017; Moreno-Rios, Tejeda-Benitez, and Bustillo-Lecompte 2022; Sang et al. 2022) and visibility (Singh, Bloss, and Pope 2017). These effects strongly depend on particle chemical composition, phase-state, size and morphology. *Effective density* is defined as the mass of a particle divided by its mobility-equivalent volume,

$$\rho_{\text{eff}} = \frac{m}{\frac{4}{3}\pi\left(\frac{d_{\text{m}}}{2}\right)^3} = \frac{6}{\pi}\frac{m}{d_{\text{m}}^3} \tag{1}$$

where m is the mass and d_{m} is the mobility-equivalent diameter of a particle. For spherical, homogeneous particles the effective density is equal to the material density (Kelly and McMurry 1992; Jimenez et al. 2003; DeCarlo et al. 2004). Effective density is an essential parameter for converting size-resolved particle number concentrations to mass-based concentrations (or total mass collected) in order to calibrate aerosol mass spectrometers (Phinney et al. 2006; Docherty et al. 2013; Schmale et al. 2013; Huang et al. 2017; Hodshire et al. 2019; Glicker et al. 2022) and to accurately estimate hygroscopic growth factors from electrodynamic balance experiments (Peng and Chan 2001; Tang et al. 2019; Guo et al. 2020). For non-spherical particles, effective density measurements provide information on particle morphology (Jimenez et al. 2003; DeCarlo et al. 2004; Zelenyuk, Cai, and Imre 2006; Olfert, Symonds, and Collings 2007). Aerosol particle effective density can also be used in concert with other measurements of particle physicochemical properties in order to infer composition (Kannosto et al. 2008; Pitz et al. 2008; Xu et al. 2020; Wang et al. 2021). Indirect methods for inferring particle composition may be particularly useful for nanometer-sized particles, given the difficulties associated with measuring their composition (Smith et al. 2021).

A common technique to determine particle effective density relies on first classifying particles with a differential mobility analyzer (DMA) and measuring in tandem their respective aerodynamic particle diameter with either a cascade impactor (Kelly and McMurry 1992; Stein et al. 1994; Ristimaki et al.

CONTACT Jason Olfert jolfert@ualberta.ca Department of Mechanical Engineering, University of Alberta, Edmonton, Alberta, Canada.
Supplemental data for this article can be accessed online at https://doi.org/10.1080/02786826.2023.2176739.
© 2023 American Association for Aerosol Research

2002), an aerodynamic aerosol classifier (Tavakoli and Olfert 2014; Yao et al. 2020; Kazemimanesh et al. 2022; Song et al. 2022), or time-of-flight methods like those found on aerosol mass spectrometers (Jimenez et al. 2003; DeCarlo et al. 2004; Bahreini et al. 2005; Zelenyuk et al. 2005; Kostenidou, Pathak, and Pandis 2007; Pratt and Prather 2012; Peng et al. 2021). In the latter case, the aerodynamic diameter measurement is made at near vacuum conditions and morphological information is required to calculate the effective density (or some will report alternative definitions of effective density based on the vacuum aerodynamic diameter which are different from the definition stated above (Jimenez et al. 2003; DeCarlo et al. 2004; Zelenyuk, Cai, and Imre 2006; Peng et al. 2021)). For example, effective densities of a series of synthesized aminium methanesulfonate salt particles were obtained from monodispersed atomized particles that were sampled using a single particle laser desorption time-of-flight mass spectrometer (Dawson et al. 2014). Particles were found to be spherical with densities values of 1310 (± 30), 1280 (± 30), 1260 (± 30) and 1320 (± 30) kg m^{-3} for ammonium, methylammonium dimethylammonium and trimethylammonium methanesulfonate, respectively.

Particle effective densities can also be derived from measurements using a combination of a DMA with a particle mass analyzer (PMA) where monodispersed particles are first classified by either mobility (DMA-PMA) or mass (PMA-DMA) (McMurry et al. 2002; Olfert et al. 2006; Johnson, Symonds, and Olfert 2013). In addition to providing effective density, these techniques can inform on particle morphology (e.g. particle shape and mass-mobility exponents) and have been applied to a wide range of particles types including soot particles (Olfert, Symonds, and Collings 2007; Pagels et al. 2009), laboratory generated secondary organic aerosol (Malloy et al. 2009) and ambient particles (Geller, Biswas, and Sioutas 2006; Rissler et al. 2014; Zhou et al. 2022). In particular, using a DMA-PMA-CPC combination, Qiu and Zhang (2012) determined effective particle densities for five atmospherically relevant alkyaminium sulfate salts covering the diameter range of 80 to 240 nm and reported that in all cases particles were spherical (mass-mobility exponent of 3).

In the present study, we report effective density particle measurements for sodium methanesulfonate (CH_3SO_3Na) and three aminium chloride salts (methylammonium chloride, monoethanolamine hydrochloride and 1,4-diaminobutane dihydrochloride) using a centrifugal particle mass analyzer (CPMA; (Olfert et al. 2006)) connected upstream of a scanning mobility particle sizer (i.e. CPMA-SMPS combination; (Malloy et al. 2009)). These salts are used here as surrogates for aminium and methanesulfonate salts present in ambient aerosols (Muller et al. 2009; Gaston et al. 2010; Smith et al. 2010; Schmale et al. 2013; Lawler et al. 2018; Hodshire et al. 2019; Sullivan et al. 2020). Because methanesulfonate has been recognized as a by-product of dimethylsulfide oxidation processes, CH_3SO_3Na particles have been previously used as a proxy for marine aerosol (Liu and Laskin 2009; Kwong et al. 2018; Tang et al. 2019; Guo et al. 2020). These salts have also commonly been used as calibration standards (Kolaitis et al. 1989; Erupe et al. 2010; Shen et al. 2017; Krempaska, Horňák, and Pernthaler 2018; Zhou et al. 2018; Feng et al. 2020; Perraud et al. 2020).

A further objective of this study is to demonstrate an alternative calibration material for effective density measurements using a PMA-DMA combination. Users of tandem PMA-DMA (or DMA-PMA) systems often use certified polystyrene latex spheres (PSL) to calibrate or verify the two classifiers (McMurry et al. 2002; Olfert et al. 2006). However, certified PSL spheres are only available in a limited range of sizes and the accumulation of surfactant or other water-based impurities on the surface of atomized PSL particles creates large uncertainties in the mass of sub 100 nm particles (Zelenyuk et al. 2005; Olfert et al. 2006; Kidd, Perraud, and Finlayson-Pitts 2014). In addition, commonly used PSL particles cannot be produced at high concentrations without coagulation (Zelenyuk, Cai, and Imre 2006). Here, Santovac® vacuum oil is proposed as an alternative calibration material and the uncertainty of the method is assessed.

2. Experimental methods

2.1. Nanoparticle generation

Particles were generated using three different generation systems presented in Figure 1. In the first system (Figure 1a), aqueous solutions of sodium chloride (NaCl; crystalline/certified ACS; Fisher Chemical), sodium methanesulfonate (CH_3SO_3Na; 98%; Aldrich), methylaminium chloride (CH_3NH_3Cl; ≥ 98%; Sigma Aldrich), monoethanolamine hydrochloride ($HO(CH_2)_2NH_2$,HCl; ≥ 99%; Sigma Aldrich) and 1,4-diaminobutane dihydrochloride ($NH_2(CH_2)_4NH_2$,2HCl; ≥ 99%; Sigma Aldrich) were atomized using a constant output atomizer (TSI, Model 3076). Solutions were made by dissolving the pure compounds into 100 mL nanopure water (18.2 MOhm-cm; Barnstead; ThermoScientific) to yield concentrations of 7.9 mM (NaCl), 2.7 mM (CH_3SO_3Na), 4.7 mM

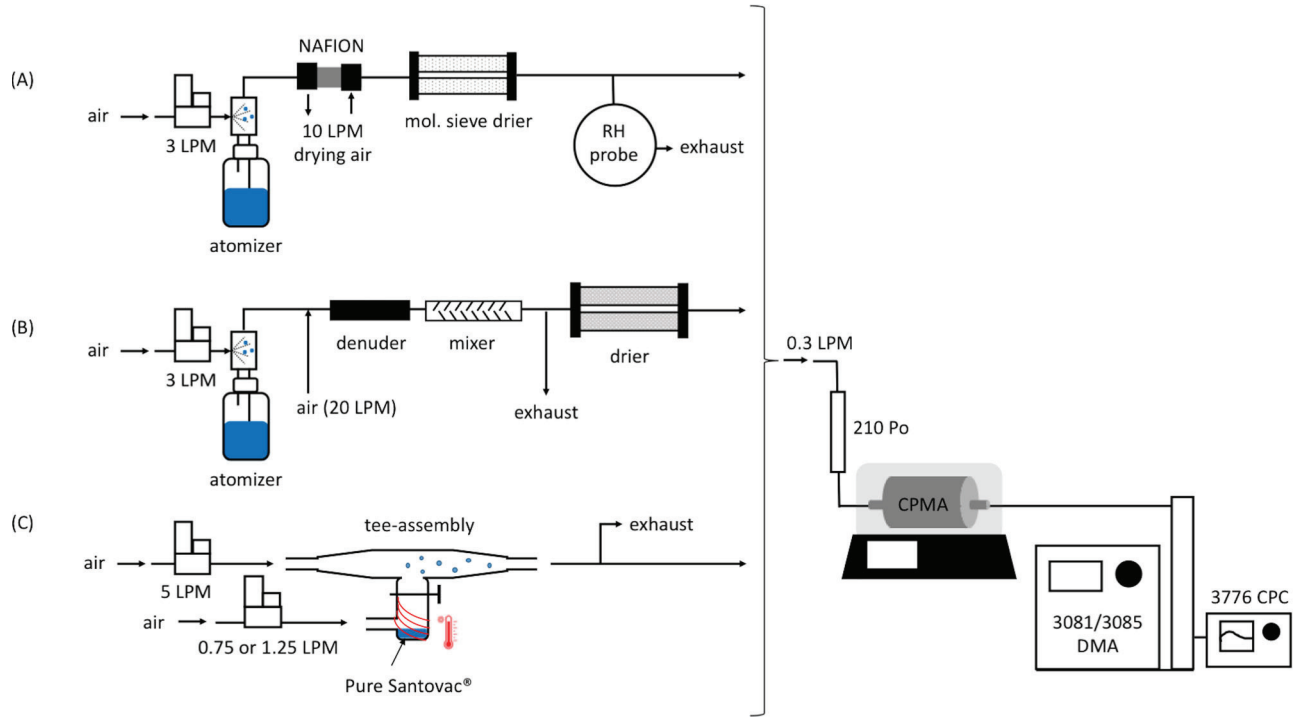

Figure 1. Experimental design used to generate particles from (A) NaCl, CH_3SO_3Na, CH_3NH_3Cl, $HO(CH_2)_2NH_2$,HCl and $NH_2(CH_2)_4NH_2$,2HCl solutions in nanopure water, (B) 0.01% Santovac® solution in acetone (v/v) and (C) pure Santovac® (homogeneous nucleation from vapor phase). The diffusion drier in (A) was filled with molecular sieve (type 13X) while the diffusion drier in (B) contained a combined carbon/alumina media. The lines (red lines) around the coater assembly represents a heating tape wrapped around the bottom section of the coater assembly.

(CH_3NH_3Cl), 3.8 mM ($HO(CH_2)_2NH_2$,HCl) and 2.2 mM ($NH_2(CH_2)_4NH_2$,2HCl). Compressed air, purified by passing through an FTIR purge air generator (Parker Balston; model 75-62), further purified through activated carbon/alumina media (PermaPure LLC) and finally an inline 0.01 micron filter (Parker Balston, type BQ) provided the air for all the experiments. Once atomized, the particles were dried using a Nafion™ drier (FC125-240-5MP-02; PermaPure; 10 L/min drying air), followed by a diffusion drier filled with molecular sieve (type 13X, Kurt J. Lesker and ACROS). Due to noticeable degradation of the Nafion™ tube, for some experiments with CH_3NH_3Cl, the system was modified (not shown) to have extra dilution air (10 L/min) downstream of the Nafion™ drier along with a static mixer (Koflo, 1/4-40-3-12-2) and an additional diffusion drier containing silica gel beads (Delta Absorbent), followed by the molecular sieve drier. In all cases, the flow of particles exiting the molecular sieve drier was then split between the instrument suite and an exhaust line. For selected experiments (NaCl and CH_3NH_3Cl), relative humidity (RH) was measured with an RH probe (Vaisala, model HMP 234) placed in the exhaust line, and was determined to be below 10%.

Calibration particles were generated from Santovac® 5 P Ultra vacuum pump fluid (Santovac Fluids LLC) by either using the atomizer (Figure 1b) or by the evaporation and homogeneous nucleation of pure Santovac® (Figure 1c). In Figure 1b, a Santovac® solution (0.01% v/v) in acetone (HPLC grade; Fisher Chemicals) was atomized, and the particles exiting the atomizer were first diluted with 20 L/min of air then passed through a carbon monolith denuder (NovaCarb™; MAST Carbon, Ltd) to remove the excess acetone. The Nafion™ tube was initially used to dry the Santovac® atomized particles; however, the membrane itself showed deterioration over time, with the membrane changing from a translucid color to black, thus it was removed from the system and replaced with the carbon monolith denuder instead to remove the excess acetone vapor. The particle stream then passed through the static mixer allowing homogeneous mixing. Excess flow was then vented and the remaining flow was sent through a supplemental diffusion drier containing carbon/alumina media to further eliminate any traces left of acetone. Eliminating acetone before the CPMA was critical to making accurate measurements since the particles can increase in temperature while being classified in the CPMA due to frictional heating due to the cylinder rotation (Titosky et al. 2019), and the evaporation of acetone from the particles during classification would bias the results. A second set of Santovac® particles were generated from nucleation

of the vapor (Figure 1c). Pure Santovac® (about 1-2 mL) was placed inside a glass tee-assembly (Wingen and Finlayson-Pitts 2019) and heated to 187-220 °C using a heating tape and variable AC transformer (Variac). The flow of air through the tee-assembly was 5 L/min through the top section of the assembly (main air flow) and 0.75 to 2 L/min through the base of the assembly, flowing in the headspace above the Santovac® fluid. Both Santovac® particle generation systems yielded similar results (Figure S1), but the second method was preferred as it was free from acetone vapors interfering with the CPMA classification.

2.2. Tandem CPMA-SMPS system

The generated particles were sent to the instrument suite, where particles were first neutralized using a ^{210}Po radioactive source (NRD LLC; model P-2021) and then mass-selected using a centrifugal particle mass analyzer (CPMA; Cambustion Ltd). Selected masses ranged from 0.01 fg up to 5 fg. The particles exiting the CPMA were then classified using a scanning mobility particle sizer (TSI, Model 30380) consisting of either a long or nano differential mobility analyzer (TSI, Model 3081 and Model 3085) and a condensation particle sizer (CPC; TSI, Model 3776). The CPC controlled the sample flow though the CPMA-SMPS system and was operated in low flow mode (0.3 L/min).

The CPMA settings (rotational speed and voltage) were kept the same for the measurement of all samples. The CPMA settings were chosen to have a mass resolution of 14 (defined as the inverse of the full-width at half-maximum of the set-point normalized transfer function) when classifying Santovac® particles (i.e. the mass (m) - mobility (d_m) relationship was entered in the CPMA software as $m = F\, d_m^3$, where F is based on the known density of Santovac® ($\rho_{true,\,Santovac}$, $1198 \pm 3\,kg\ m^{-3}$; (Tajima et al. 2013)); $F = \frac{\pi}{6} \times 1198\,kg\ m^{-3} = 627.3\,kg\ m^{-3}$).

The SMPS settings were adjusted based on the size of CPMA-classified particles to be measured. Particles with masses of 0.01 to 0.065 fg used the nano DMA with a sheath flow of 15 L/min (resulting in a mobility resolution of 50); particles with masses of 0.15 to 0.9 fg used the nano DMA with a sheath flow of 3 L/min (mobility resolution of 10); and particles with masses of 2 to 5 fg used the long DMA with a sheath flow of 3 L/min (mobility resolution of 10). The SMPS was set to scan for 1 min only over the range of sizes exiting the CPMA in order to reduce errors due to transient effects in the SMPS (e.g. for 0.01 fg Santovac® particles, the SMPS was scanned over the range of 23.3 to 27.9 nm). At least 5 SMPS scans were completed for each CPMA set point.

For both CH_3NH_3Cl and $HO(CH_2)_2NH_2$,HCl particles, it was necessary to cool down the CPMA to temperatures below ambient (between 15 °C and 25 °C) in between each measurement as these particles tended to evaporate inside the instrument. This was accomplished by placing ice bags around the CPMA cylinder as well as flowing cold air inside the instrument (8 L/min). The air was cooled by passing it through a glass column containing ethylene glycol maintained at temperature $<$ 0 °C using a recirculating temperature-controlled bath (NESLAB; model RTE-111).

3. Data analysis and uncertainties

In the tandem CPMA-SMPS measurements, the effective density of a particle (Equation (1)) was calculated where m was the CPMA mass set point and d_m was the median diameter of a lognormal fit of the SMPS number-weighted mobility diameter distribution (where the number distribution was provided by the TSI AIM software (version 9) and the lognormal fit was provided by Matlab or Igor Pro).

Since the effective density scales with the cube of the mobility diameter, small errors in the measurement of d_m result in large errors in effective density. A carefully calibrated DMA has an uncertainty of ~3.3% (Kinney et al. 1991) and a CPMA has an uncertainty of ~1.4% (Symonds, Reavell, and Olfert 2013). The uncertainty in density given uncertainties in mass and mobility diameter is

$$\frac{u_{\rho_{eff}}}{\rho_{eff}} = \sqrt{\left(\frac{u_m}{m}\right)^2 + 9\left(\frac{u_{d_m}}{d_m}\right)^2}. \quad (2)$$

Thus, simply calibrating the instruments would result in an uncertainty of at least 10% ($\frac{u_{\rho_{eff}}}{\rho_{eff}} = \sqrt{(0.014)^2 + 9(0.033)^2} = 0.10$) not including additional errors due to scanning of the SMPS, SMPS data inversion, and fitting the SMPS data. Therefore, it is good practice to calibrate the system as a whole in terms of effective density in addition to calibrating each instrument. This is done by measuring the effective density of a particle with a spherical shape and known material density to determine a calibration factor ($K(d_m)$) between the measured density of the calibration particle ($\rho_{meas,\,Santovac}(d_m)$) and the true material density ($\rho_{true,\,Santovac}$) for each particle diameter (d_m) as:

$$K(d_m) = \frac{\rho_{meas,\,Santovac}(d_m)}{\rho_{true,\,Santovac}} = \frac{\frac{6}{\pi}\frac{m_{CPMA}}{d^3_{m,\,DMA}}}{\rho_{true,\,Santovac}} \quad (3)$$

where m_{CPMA} is the particle mass measured by the mass classifier (CPMA) and $d_{m,DMA}$ is the mobility diameter measured by the DMA. The tandem CPMA-SMPS measurements are then carried out on the particles of interest (salt particles in this work) using the same CPMA and SMPS settings and the effective density measurements ($\rho_{eff,\,meas}(d_m)$) for each particle diameter d_m are corrected by the calibration factor to determine the best estimate of the true effective density ($\rho_{eff,\,corr}(d_m)$),

$$\rho_{eff,\,corr}(d_m) = \frac{\rho_{eff,\,meas}(d_m)}{K(d_m)} = \frac{\frac{6}{\pi}\frac{m_{CPMA}}{d^3_{m,\,DMA}}}{K(d_m)}. \quad (4)$$

In the past, polystyrene latex spheres (PSL) have been used for the calibration particles (e.g (McMurry et al. 2002; Olfert et al. 2006)). However, the use of PSL has several drawbacks: i) surfactant and other water impurities remain on the surface of dried PSL particles resulting in particles with densities that differ from pure PSL (Knollenberg 1989) and may also cause the particles to become non-spherical (Zelenyuk et al. 2005). Although steps can be taken to minimize the amount of surfactant (e.g. (Kidd, Perraud, and Finlayson-Pitts 2014), all impurities cannot be removed and this is especially problematic for PSL particles smaller than 100 nm in diameter where the amount of residual material is proportionally larger. ii) PSL is only available in discrete sizes. iii) As PSL particles have a relatively narrow size distribution, some care needs to be taken to set the first classifier in the system (CPMA or DMA) to select the peak of the PSL distribution otherwise the distribution exiting the classifier will be nonsymmetrical and will introduce biases in the data fitting.

Alternatively, a liquid particle of known density can be used for calibration. A few low volatility liquids have been used as benchmarks for effective density measurements, such as dioctylphthalate (DOP) (Zelenyuk et al. 2005; Malloy et al. 2009), dioctyl sebacate (DOS) (McMurry et al. 2002; Tavakoli and Olfert 2014) and fluorinated lubricant Fomblin® (McMurry et al. 2002; Zelenyuk et al. 2005). Here we use Santovac® 5 P Ultra vacuum pump fluid (Santovac Fluids, Inc.) as the calibration particle. Santovac® (1,3-bis(3-phenoxyphenoxy)-benzene, $C_{30}H_{22}O_4$ (National Center for Biotechnology Information)) is a five ring polyphenyl ether molecule with a molecular weight of 446.5 g mol^{-1}, and has a very low vapor pressure (4×10^{-10} Torr; (Scientific Instrument Services (SIS)), which is much lower that the vapor pressures of the liquids mentioned above) and known density (1198 ± 3 kg m^{-3}; (Tajima et al. 2013)), which is close to that of the salts studied here. As such Santovac® is nonvolatile and is well suited to be a reference material for this study. Also, Santovac® particles can be generated by atomizing a solution in acetone or by evaporating and nucleating pure Santovac®; the latter producing Santovac® particles with a negligible amount of impurities. The size distribution of the Santovac® aerosol is very broad (Figure S2) so a wide range of particles can be used for calibration.

Figure 2 shows the effective density measurements of Santovac® particles with the CPMA-SMPS system as a function of mobility diameter. The error bars represent the 95% confidence interval of the uncertainty in the mean of the measurements and at least 5 measurements were taken for each data point. Two calibration curves are shown: Calibration 1 are measurements taken after the first calibration of the DMA sheath flow and Calibration 2 are measurements taken after a second calibration of the DMA sheath flow.

Calibration 1 contains data where Santovac® particles were generated by atomization of a Santovac®/acetone solution as well as through the evaporation and homogeneous nucleation of pure Santovac®. This data was combined because there was little difference observed between the effective density measurements of the two methods (Figure S1). However, it should be noted that some effective density measurements of the Santovac®/acetone particles were unrepeatable, presumably due to the fact that the acetone was not completely evaporated before entering the CPMA where further evaporation took place because the particles were warmed in the

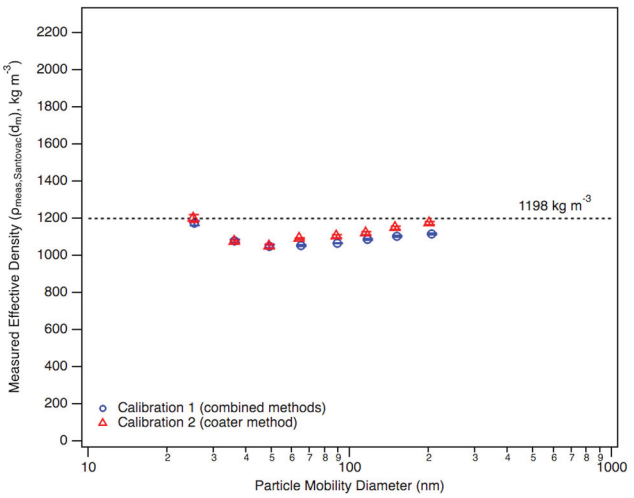

Figure 2. Effective density measurement of Santovac® particles with the CPMA-SMPS system ($\rho_{meas,\,Santovac}(d_m)$). Error bars represent the uncertainty of the mean of repeated measurements with 95% confidence.

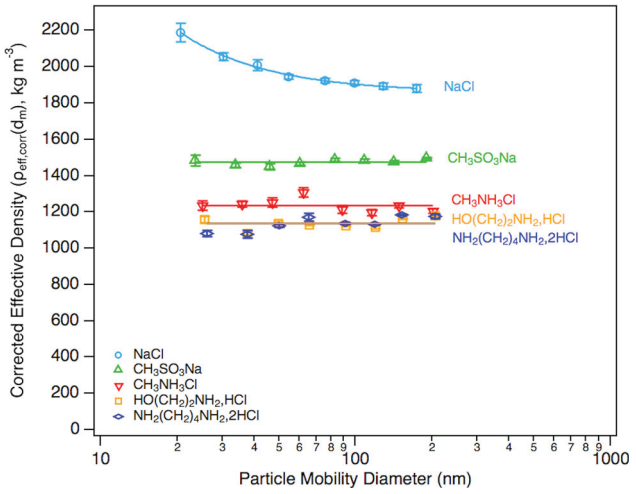

Figure 3. Corrected effective density ($\rho_{eff,corr}(d_m)$) of salt particles as a function of their mobility diameter. Error bars represent the uncertainty in the CPMA-SMPS measurement with 95% confidence. The straight lines on the figure represent the average corrected effective density, while the line on the NaCl data is a power-law fit. The measured effective densities were corrected using the Santovac® calibration factor (K(d_m)) using Equation (3).

CPMA as it rotated. Therefore, it is recommended that evaporated and nucleated Santovac® be used to avoid this issue and also to lower the amount of impurities in the Santovac® particles.

Although all data points are within 13% of the true material density of Santovac®, they are systematically lower due to biases in: i) the classifiers: classifier voltages, classifier dimensions (radial dimensions in the CPMA and DMA, and length in the DMA), DMA sheath flow, and CPMA rotational speed; ii) the measurement method: SMPS scanning artifacts, SMPS data inversion and fitting; or iii) aerosol properties: impurities in the Santovac® particles due to incomplete evaporation of acetone. All of the classifier and measurement method biases (i and ii) can be corrected by the calibration method, thus effective density measurements with accuracies much better than 10% are possible. The role of impurities (iii) was tested by generating the aerosol with two methods (nucleation and atomization) with the same sheath flow calibration as illustrated in Figure S1. The purity of Santovac® 5 P Ultra is >99% so the nucleation of the oil should result in uncertainties in density <1%. The atomization of the Santovac®/acetone solution would result in higher impurities due to additional impurities in the acetone (or the presence of acetone that would not have evaporated completely), however, the good agreement between the two generation methods can exclude the presence of impurities as the cause of the bias in the measurements. As further evidence, but not proof, the uncorrected effective density curves of the salts have a similar shape as the Santovac® curve (i.e. minimum density near 40–50 nm as shown in Figure S6) suggesting the bias is due to the classifiers and method rather than impurities in the Santovac®.

Equation (2) shows that a 4.3% error in the diameter measurement with the DMA would result in a 13% error in density if error in the CPMA is neglected. The diameter measurement of the DMA is determined by,

$$d_m = \frac{2qVLC_c}{3\mu Q_{sh}\ln\left(\frac{r_2}{r_1}\right)} \tag{5}$$

where q is the electric charge on the particle, C_c is the slip correction factor, V is voltage, L is the length of the classifier, μ is the viscosity of the gas, Q_{sh} is the sheath flow, and r_2 and r_1 are the outer and inner diameter of the classifier. Therefore, a 6% error in radii (highly unlikely), or a 4.3% error any of the other parameters, or combination of errors in those parameters, would result in 13% error in density. Kinney et al. (1991) show that the major sources of error in the DMA are the sheath flow and slip correction factor (in their study all sources of error resulted in an uncertainty 3.3% in diameter measurement). The effect of the error in the sheath flow is observed in our results as well as the two calibrations of sheath flow resulted in different densities (Figure 2). Additional errors will be introduced by scanning the SMPS to determine the median particle diameter and Duelge et al. (2022) estimate this causes an additional uncertainty on the order of ~1%. In our work, SMPS measurements were performed with high resolution (Figure S3) to reduce scanning errors and the inverted results show no difference when correcting the SMPS data for multiple charges and diffusion (Figure S4).

The mean mass of the particles exiting the CPMA is determined by,

$$m = \frac{qV}{\left(\frac{r_2+r_1}{2}\right)^2\omega^2\ln\left(\frac{r_2}{r_1}\right)} \tag{6}$$

where ω is the mean rotational speed of the CPMA. A 13% error in density would require a 13% error in the mass measurement if there was no error in the DMA (see Equation (2)). This would require a 13% in voltage, a 6.5% error in rotational speed, or a 0.2% error in radii (see Symonds, Reavell, and Olfert (2013) for a detailed analysis). The importance of radii on uncertainty is due the small gap between the cylinders which causes error in the electrostatic force.

It is important to note that the error in the density measurement will likely come from both the DMA

and the CPMA. Moreover, it is expected that the errors would depend on the mass or diameter measured, as the values of some parameters change as a function of mass or diameter; in particular: sheath flow (15 LPM or 3 LPM), voltages, rotational speed and DMA dimensions (long and nano DMA were both used). Thus, a different calibration factor was calculated at each CPMA/DMA set point (Equation (3)). Each calibration curve was used to correct the data obtained using the same DMA sheath flow. Calibration 1 was used for the CH_3SO_3Na, $HO(CH_2)_2NH_2$,HCl, $NH_2(CH_2)_4NH_2$,2HCl and the 0.01 and 0.0269 fg CH_3NH_3Cl data, while Calibration 2 was used for the NaCl and remaining CH_3NH_3Cl data. Figure S5 presents the calibration factor (K_{d_m}) experimentally determined for each calibration set.

The uncertainty in the effective density measurement using the calibration factor can be found by propagating the uncertainty in the calibration and the uncertainties in the measurements. The uncertainty in the calibration factor (U_K) includes the uncertainty in the density of the Santovac® (± 3 kg m^{-3}) and the uncertainty in the mean of the repeated CPMA-SMPS measurements of the Santovac® (i.e. the "precision" or "Type A" uncertainty; $P_{\rho_{\text{meas, Santovac}}(d_\text{m})}$)

$$U_K = K(d_\text{m})\sqrt{\left(\frac{P_{\rho_{\text{meas, Santovac}}(d_\text{m})}}{\rho_{\text{meas, Santovac}}(d_\text{m})}\right)^2 + \left(\frac{3\ \text{kg m}^{-3}}{1198\ \text{kg m}^{-3}}\right)^2} \tag{7}$$

where

$$P_{\rho_{\text{meas, Santovac}}(d_\text{m})} = t\frac{S_x}{\sqrt{n}} \tag{8}$$

where S_x is the standard deviation of the measurements, n is the number of measurements taken, and t is value of the t-distribution for the desired confidence level (95% used in this work).

The uncertainty in the subsequent effective density measurement of the salts ($U_{\rho_{\text{eff, corr, dm}}}$) will then be

$$U_{\rho_{\text{eff, corr}}(d_\text{m})} = \rho_{\text{eff, corr}}(d_\text{m})\sqrt{\left(\frac{P_{\rho_{\text{eff, corr}}(d_\text{m})}}{\rho_{\text{eff, corr}}(d_\text{m})}\right)^2 + \left(\frac{U_K}{K(d_\text{m})}\right)^2}. \tag{9}$$

4. Results and discussion

Figure 3 shows the corrected effective density values experimentally determined for the five salts studied where the error bars show the uncertainty calculated in Equation (9). For completeness, the raw measured effective densities before correction can be found in Figure S6 (and typical size distribution recorded for the polydisperse salt particles are in Figure S2 B–F). Figure 3 shows that the CH_3SO_3Na, CH_3NH_3Cl, $HO(CH_2)_2NH_2$,HCl, and $NH_2(CH_2)_4NH_2$,2HCl particles do not have a size-dependent effective density. This implies that the particles are spherical with a constant (non-size dependent) material density. In support of that, the mass-mobility relationship experimentally determined for each of the systems studied is represented in Figure S7 and show that with the exception of NaCl particles, all particles studied exhibit a mass-mobility exponent of 3 associated with perfect spheres. Note that a size-independent effective density is also possible for non-spherical particles with an approximately size-independent dynamic shape factor and the effective density will not equal the material density for spherical particles if internal voids are present. However, it is unlikely the non-NaCl particles were non-spherical or had internal voids as others have investigated their structure. In particular, Liu and Laskin (2009), using transmission electron microscopy, showed that submicron dried CH_3SO_3Na particles were spherical with clear contour and likely adopted a crystalline phase, with a deliquescence point of 71% RH and an efflorescence of 49% RH. Also, Belusso et al. (2021) showed that the hydrochloride salts are semi-volatile (in particular CH_3NH_3Cl and $HO(CH_2)_2NH_2$,HCl, consistent with thermogravimetry reports) and thus they likely form spherical particles without voids. The straight lines on the figure show the average effective density of each salt over the range of particles sizes measured. Note that some data points deviate from the average effective density by a value greater than the uncertainty in the measurement. While the Santovac® calibration greatly reduces biases in the measurements, it does not account for errors which are caused by physical changes in the particles as they are measured in the CPMA-SMPS system. Specifically, particles in the CPMA are warmed due to frictional heating of the rotating cylinders (Titosky et al., 2019). Thus, material from the particles may evaporate while they are classified by the CPMA. This material maybe the salt material itself or water in the particle if the particle was not sufficiently dried before entering the CPMA. This effect is illustrated in Figure S8 for CH_3NH_3Cl taken as an example, where a clear trend is visible for the residuals (taken as the difference between the corrected effective density ($\rho_{\text{eff, corr}}(d_\text{m})$) and the average effective density) and the CPMA temperature for the 0.015

Table 1. Average effective density estimated for CH_3SO_3Na, CH_3NH_3Cl, $HO(CH_2)_2NH_2$,HCl and $NH_2(CH_2)_4NH_2$,2HCl salt nanoparticles. The uncertainties only represent uncertainty in the mean value of the measurements (only the precision uncertainty, 95% confidence interval).

	Effective Density (kg m^{-3})	Literature Values (kg m^{-3})
CH_3SO_3Na	1474 ± 13	1568 (Peng and Chan 2001) 1955 (Tang et al. 2019)
CH_3NH_3Cl	1236 ± 29	1230 (Hendricks 1928) 1216 (Hughes and Lipscomb 1946)
$HO(CH_2)_2NH_2$,HCl	1136 ± 26	1380 (Koo, Lee, and Shin 1972)
$NH_2(CH_2)_4NH_2$,2HCl	1135 ± 33	1310 (VWR)

fg series. As seen in Figure 3, the scatter of the low volatility salts (NaCl and CH_3SO_3Na) around the average value is relatively small compared to the semi-volatile salts (CH_3NH_3Cl, $HO(CH_2)_2NH_2$,HCl, and $NH_2(CH_2)_4NH_2$,2HCl), which suggests that particle volatility leads to increased uncertainty in the measurements.

Table 1 shows the average effective densities for the CH_3SO_3Na, CH_3NH_3Cl, $HO(CH_2)_2NH_2$,HCl and $NH_2(CH_2)_4NH_2$,2HCl particles. The uncertainties only represent uncertainty in the mean value of the measurements (only the precision uncertainty) as the bias uncertainty in the measurements (Equation (9)) is small in comparison. There have been only limited density measurements for these salts in the literature, with some discrepancies between them. For example, Peng and Chan reported a bulk material density of 1568 kg m^{-3} measured at 25 °C for CH_3SO_3Na based on a dry solute measurement (Peng and Chan 2001), while Tang and coworkers (2019) reported a value of 1955 kg m^{-3} using a gas pycnometer. Our effective density measurement is close to the one reported by Peng and Chan (2001) with a difference of only 94 kg m^{-3} (~6% difference) while it differs significantly from the Tang et al. (2019) value (481 kg m^{-3} corresponding to a ~33% difference). It is important to note that these two reported values refer to bulk material densities, while our measurement is a direct particle effective density measurement (which is the property of interest for aerosol applications). For CH_3NH_3Cl, available density values were estimated in two separate studies from the crystal structure of the salt with relatively close density values of 1230 kg m^{-3} (Hendricks 1928) and 1216 kg m^{-3} (Hughes and Lipscomb 1946), respectively, where two CH_3NH_3Cl molecules exist in one unit cell. Our measurements are in good agreement with these values. Koo et al. (1972) determined the density for a single $HO(CH_2)_2NH_2$,HCl crystal in benzene and carbon tetrachloride to be 1380 kg m^{-3} using the sink-and-float method. Lastly, the only available density for $NH_2(CH_2)_4NH_2$,2HCl is its bulk material density provided by its manufacturer (VWR). For both of these salts, our direct effective particle density values are similar, but systematically lower than that reported for the bulk material densities by about 13-18%.

Figure 3 also shows that the effective density of NaCl is not constant with respect to mobility diameter. This is due to the fact that the NaCl particles are non-spherical. It is well known that nanoparticles of atomized NaCl tend to have a cube-like shape (Park et al., 2009) although the shape of the particle depends on the rate at which the particle is dried (Zelenyuk, Cai, and Imre 2006; Wang et al. 2010). Since the effective density of the particles depends on drying rate, it is difficult to compare our results with others. However, previous researchers measuring effective density of atomized and diffusion-dried NaCl (Zelenyuk, Cai, and Imre 2006) and flame-generated NaCl (Sipkens et al. 2021) have reported very similar effective densities and have shown that the effective density of NaCl approaches the material density of NaCl at small sizes (2170 kg m^{-3}; (Rumble, 2022)) and decreases as the mobility diameter increases. A fit of the NaCl effective density (to within 1% of the data) as a function of mobility diameter gives

$$\rho_{\text{eff, NaCl}} = 1859 \text{ kg m}^{-3} + 14498 \left(\text{kg m}^{-3} \text{ nm}^{1.2509}\right) d_{\text{m}}^{-1.2509}. \quad (10)$$

However, it should be stated that care should be taken in extrapolating this relation as it gives effective densities higher than the material density for mobility diameters below 22 nm.

It is often convenient to represent the effective density data as a mass-mobility relationship using a power law. A fit of the mass-mobility data for NaCl nanoparticles (within 4% of the data) gives:

$$m = 345 \text{ (kg m}^{-2.934}) d_{\text{m}}^{2.934}. \quad (11)$$

Conclusion

The effective density of five salts important for atmospheric science were measured over the mobility diameter range of 20 – 200 nm using a tandem CPMA-SMPS system. Our measurements identified some challenges that are unique to nanoparticle

density measurements and are related to the high rotational speeds needed to mass-select these particles using the CPMA. This can result in higher temperatures within the CPMA and must be mitigated in order to ensure that particles do not evaporate, the latter being particularly important for nanometer sized particles given that these particles could be more volatile due to the Kelvin effect. We also demonstrated that the accuracy of effective density measurements using the tandem CPMA-SMPS approach can be improved by calibrating the tandem CPMA-SMPS system with particles generated from Santovac® vacuum fluid. Santovac® calibration particles showed important advantages over PSL particles, specifically in the ability to generate chemically pure particles and the flexibility in selecting any sample size or mass rather than discrete sizes.

Acknowledgments

The authors would like to thank Prof. Heejung Jung University of California Riverside for lending us the CPMA for these experiments.

Disclosure statement

No potential conflict of interest was reported by the authors.

Funding

The authors are grateful to the National Science Foundation (Grants No. 1928252 and CHE-2004066) and the Natural Science and Engineering Research Council of Canada for supporting this research.

ORCID

Véronique Perraud http://orcid.org/0000-0003-1247-9787
James N. Smith http://orcid.org/0000-0003-4677-8224
Jason Olfert http://orcid.org/0000-0002-9681-5428

References

Bahreini, R., M. D. Keywood, N. L. Ng, V. Varutbangkul, S. Gao, R. C. Flagan, J. H. Seinfeld, D. R. Worsnop, and J. L. Jimenez. 2005. Measurements of secondary organic aerosol from oxidation of cycloalkenes, terpenes, and m-xylene using an Aerodyne aerosol mass spectrometer. *Environ. Sci. Technol.* 39 (15):5674–88. doi:10.1021/es048061a.

Belusso, A. C., M. L. Strack, G. P. M. da Silva, R. D. Soares, and P. B. Staudt. 2021. Vapor-liquid equilibrium pressure of ethanolamine hydrochloride, and vapor-solid equilibrium pressure of methylamine, pyridine, and trimethylamine hydrochlorides by thermogravimetric method. *Braz. J. Chem. Eng.* 38 (2):411–20. doi:10.1007/s43153-020-00086-y.

Dawson, M. L., M. E. Varner, V. Perraud, M. J. Ezell, J. Wilson, A. Zelenyuk, R. B. Gerber, and B. J. Finlayson-Pitts. 2014. Amine-amine exchange in aminium-methanesulfonate aerosols. *J. Phys. Chem. C* 118 (50):29431–40. doi:10.1021/jp506560w.

DeCarlo, P. F., J. G. Slowik, D. R. Worsnop, P. Davidovits, and J. L. Jimenez. 2004. Particle morphology and density characterization by combined mobility and aerodynamic diameter measurements. Part 1: Theory. *Aerosol Sci. Tech.* 38 (12):1185–205. doi:10.1080/027868290903907.

Docherty, K. S., M. Jaoui, E. Corse, J. L. Jimenez, J. H. Offenberg, M. Lewandowski, and T. E. Kleindienst. 2013. Collection efficiency of the aerosol mass spectrometer for chamber-generated secondary organic aerosols. *Aerosol Sci. Tech.* 47 (3):294–309. doi:10.1080/02786826.2012.752572.

Duelge, K., G. Mulholland, M. Zachariah, and V. A. Hackley. 2022. Accurate nanoparticle size determination using electrical mobility measurements in the step and scan modes. *Aerosol Sci. Tech.* 56 (12):1096–113. doi:10.1080/02786826.2022.2128986.

Erupe, M. E., A. Liberman-Martin, P. J. Silva, Q. G. J. Malloy, N. Yonis, D. R. Cocker, and K. L. Purvis-Roberts. 2010. Determination of methylamines and trimethylamine-N-oxide in particulate matter by non-suppressed ion chromatography. *J. Chromatogr. A* 1217 (13):2070–3. doi:10.1016/j.chroma.2010.01.066.

Feng, H., X. N. Ye, Y. X. Liu, Z. K. Wang, T. X. Gao, A. Y. Cheng, X. F. Wang, and J. M. Chen. 2020. Simultaneous determination of nine atmospheric amines and six inorganic ions by non-suppressed ion chromatography using acetonitrile and 18-crown-6 as eluent additive. *J. Chromatogr. A* 1624:461234. ARTN 461234. doi:10.1016/j.chroma.2020.461234.

Gaston, C. J., K. A. Pratt, X. Y. Qin, and K. A. Prather. 2010. Real-time detection and mixing state of methanesulfonate in single particles at an inland urban location during a phytoplankton bloom. *Environ. Sci. Technol.* 44 (5):1566–72. doi:10.1021/es902069d.

Geller, M., S. Biswas, and C. Sioutas. 2006. Determination of particle effective density in urban environments with a differential mobility analyzer and aerosol particle mass analyzer. *Aerosol Sci. Tech.* 40 (9):709–23. doi:10.1080/02786820600803925.

Glicker, H. S., M. J. Lawler, S. Chee, J. Resch, L. A. Garofalo, K. J. Mayer, K. A. Prather, D. K. Farmer, and J. N. Smith. 2022. Chemical composition of ultrafine sea spray aerosol during the Sea Spray Chemistry and Particle Evolution Experiment. *Acs Earth Space Chem.* 6 (7):1914–23. doi:10.1021/acsearthspacechem.2c00127.

Guo, L. Y., C. Peng, T. M. Zong, W. J. Gu, Q. X. Ma, Z. J. Wu, Z. Wang, X. Ding, M. Hu, X. M. Wang, et al. 2020. Comprehensive characterization of hygroscopic properties of methanesulfonates. *Atmos Environ* 224:117349. ARTN 117349, doi:10.1016/j.atmosenv.2020.117349.

Heal, M. R., P. Kumar, and R. M. Harrison. 2012. Particles, air quality, policy and health. *Chem. Soc. Rev.* 41 (19):6606–30. doi:10.1039/c2cs35076a.

Hendricks, S. 1928. V. The crystal structures of the monomethyl ammonium halides. *Z. Fur Krist. - Cryst. Mater.* 67 (1-6):106–18. doi:10.1524/zkri.1928.67.1.106.

Hodshire, A. L., P. Campuzano-Jost, J. K. Kodros, B. Croft, B. A. Nault, J. C. Schroder, J. L. Jimenez, and J. R. Pierce. 2019. The potential role of methanesulfonic acid (MSA) in aerosol formation and growth and the associated radiative forcings. *Atmos. Chem. Phys.* 19 (5):3137–60. doi:10.5194/acp-19-3137-2019.

Huang, S., L. Poulain, D. van Pinxteren, M. van Pinxteren, Z. J. Wu, H. Herrmann, and A. Wiedensohler. 2017. Latitudinal and seasonal distribution of particulate MSA over the Atlantic using a validated quantification method with HR-ToF-AMS. *Environ. Sci. Technol.* 51 (1):418–26. doi:10.1021/acs.est.6b03186.

Hughes, E. W., and W. N. Lipscomb. 1946. The crystal structure of methylammonium chloride. *J. Am. Chem. Soc.* 68 (10):1970–5. doi:10.1021/ja01214a029.

IPCC Climate Change. 2021. The Physical Science Basis. Contribution of Working Group I to the Sixth Assessment Report of the Intergovernmental Panel on Climate Change. Cambridge University Press, United Kingdom and New York, NY, USA, 2391 pp.

Jimenez, J. L., R. Bahreini, D. R. Cocker, H. Zhuang, V. Varutbangkul, R. C. Flagan, J. H. Seinfeld, C. D. O'Dowd, and T. Hoffmann. 2003. New particle formation from photooxidation of diiodomethane (CH_2I_2). *J. Geophys. Res.-Atmos.* 108 (D10) Artn 4318:1–25. doi:10.1029/2002jd002452.

Johnson, T. J., J. P. R. Symonds, and J. S. Olfert. 2013. Mass-mobility measurements using a centrifugal particle mass analyzer and differential mobility spectrometer. *Aerosol Sci. Tech.* 47 (11):1215–25. doi:10.1080/02786826.2013.830692.

Kannosto, J., A. Virtanen, M. Lemmetty, J. M. Makela, J. Keskinen, H. Junninen, T. Hussein, P. Aalto, and M. Kulmala. 2008. Mode resolved density of atmosphreic aerosol particles. *Atmos. Chem. Phys.* 8 (17):5327–37. doi:10.5194/acp-8-5327-2008.

Kazemimanesh, M., M. M. Rahman, D. Duca, T. J. Johnson, A. Addad, G. Giannopoulos, C. Focsa, and A. M. Boies. 2022. A comparative study on effective density, shape factor, and volatile mixing of non-spherical particles using tandem aerodynamic diameter, mobility diameter, and mass measurements. *J. Aerosol. Sci.* 161:105930. ARTN 105930, doi:10.1016/j.jaerosci.2021.105930.

Kelly, W. P., and P. H. McMurry. 1992. Measurement of particle density by inertial classification of differential mobility analyzer generated monodisperse aerosols. *Aerosol Sci. Tech.* 17 (3):199–212. doi:10.1080/02786829208959571.

Kidd, C., V. Perraud, and B. J. Finlayson-Pitts. 2014. Surfactant-free latex spheres for size calibration of mobility particle sizers in atmospheric aerosol applications. *Atmos. Environ.* 82:56–9. doi:10.1016/j.atmosenv.2013.09.056.

Kinney, P. D., D. Y. H. Pui, G. W. Mulliolland, and N. P. Bryner. 1991. Use of the electrostatic classification method to size 0.1 um SRM particles – A feasibility study. *J. Res. Natl. Inst. Stand. Technol.* 96 (2):147–76. doi:10.6028/jres.096.006.

Knollenberg, R. G. 1989. The measurement of latex particle sizes using scattering ratios in the rayleigh-scattering size range. *J. Aerosol Sci.* 20 (3):331–45. doi:10.1016/0021-8502(89)90008-6.

Kolaitis, L. N., F. J. Bruynseels, R. E. Van Grieken, and M. O. Andreae. 1989. Determination of methanesulfonic-acid and non-sea-salt sulfate in single marine aerosol-particles. *Environ. Sci. Technol.* 23 (2):236–40. doi:10.1021/es00179a018.

Koo, C. H., O. Lee, and H. S. Shin. 1972. The crystal structure of monoethanolamine hydrochloride. *J. Korean Chem. Soc.* 16:6–12.

Kostenidou, E., R. K. Pathak, and S. N. Pandis. 2007. An algorithm for the calculation of secondary organic aerosol density combining AMS and SMPS data. *Aerosol Sci Tech* 41 (11):1002–10. doi:10.1080/02786820701666270.

Krempaska, N., K. Horňák, and J. Pernthaler. 2018. Spatiotemporal distribution and microbial assimilation of polyamines in a mesotrophic lake. *Limnol. Oceanogr.* 63 (2):816–32. doi:10.1002/lno.10672.

Kwong, K. C., M. M. Chim, E. H. Hoffmann, A. Tilgner, H. Herrmann, J. F. Davies, K. R. Wilson, and M. N. Chan. 2018. Chemical transformation of methanesulfonic acid and sodium methanesulfonate through heterogeneous OH oxidation. *ACS Earth Space Chem.* 2 (9):895–903. doi:10.1021/acsearthspacechem.8b00072.

Lawler, M. J., M. P. Rissanen, M. Ehn, R. L. Mauldin, N. Sarnela, M. Sipila, and J. N. Smith. 2018. Evidence for diverse biogeochemical drivers of boreal forest new particle formation. *Geophys. Res. Lett.* 45 (4):2038–46. doi:10.1002/2017GL076394.

Lelieveld, J. 2017. Clean air in the Anthropocene. *Faraday Discuss.* 200:693–703. doi:10.1039/c7fd90032e.

Lelieveld, J., J. S. Evans, M. Fnais, D. Giannadaki, and A. Pozzer. 2015. The contribution of outdoor air pollution sources to premature mortality on a global scale. *Nature* 525 (7569):367–71. doi:10.1038/nature15371.

Liu, Y., and A. Laskin. 2009. Hygroscopic properties of CH_3SO_3Na, CH_3SO_3. NH_4, $(CH_3SO_3)_2Mg$, and $(CH_3SO_3)_2Ca$ particles studied by micro-FTIR spectroscopy. *J. Phys. Chem. A* 113 (8):1531–8. doi:10.1021/jp8079149.

Malloy, Q. G. J., S. Nakao, L. Qi, R. Austin, C. Stothers, H. Hagino, and D. R. Cocker. 2009. Real-time aerosol density determination utilizing a modified scanning mobility particle sizer aerosol particle mass analyzer system. *Aerosol Sci. Tech.* 43 (7):673–8. doi:10.1080/02786820902832960.

McMurry, P. H., X. Wang, K. Park, and K. Ehara. 2002. The relationship between mass and mobility for atmospheric particles: A new technique for measuring particle density. *Aerosol Sci. Tech.* 36 (2):227–38. doi:10.1080/027868202753504083.

Moreno-Rios, A. L., L. P. Tejeda-Benitez, and C. F. Bustillo-Lecompte. 2022. Sources, characteristics, toxicity, and control of ultrafine particles: An overview. *Geosci Front* 13 (1):101147. ARTN 101147. doi:10.1016/j.gsf.2021.101147.

Muller, C., Y. Iinuma, J. Karstensen, D. van Pinxteren, S. Lehmann, T. Gnauk, and H. Herrmann. 2009. Seasonal variation of aliphatic amines in marine sub-micrometer particles at the Cape Verde islands. *Atmos. Chem. Phys.* 9 (24):9587–97. doi:10.5194/acp-9-9587-2009.

National Center for Biotechnology Information PubChem Compound Summary for CID 75565, 1,3-Bis(3-phenoxyphenoxy)benzene. 2022. https://pubchem.ncbi.nlm.nih.gov/compound/1_3-Bis_3-phenoxyphenoxy_benzene (last visited Nov. 25).

Olfert, J. S., K. S. J. Reavell, M. G. Rushton, and N. Collings. 2006. The experimental transfer function of the Couette centrifugal particle mass analyzer. *J. Aerosol Sci.* 37 (12):1840–52. doi:10.1016/j.jaerosci.2006.07.007.

Olfert, J. S., J. P. R. Symonds, and N. Collings. 2007. The effective density and fractal dimension of particles emitted from a light-duty diesel vehicle with a diesel oxidation catalyst. *J. Aerosol Sci.* 38 (1):69–82. doi:10.1016/j.jaerosci.2006.10.002.

Pagels, J., A. F. Khalizov, P. H. McMurry, and R. Y. Zhang. 2009. Processing of soot by controlled sulphuric acid and water condensation mass and mobility relationship. *Aerosol Sci. Tech.* 43 (7):629–40. doi:10.1080/02786820902810685.

Park, K., J.-S. Kim, and A. L. Miller. 2009. A study on effects of size and structure on hygroscopicity of nanoparticles using tandem differential mobility analyzer and TEM. *J. Nanopart. Res.* 11 (1):175–83. doi:10.1007/s11051-008-9462-4.

Peng, C. G., and C. K. Chan. 2001. The water cycles of water-soluble organic salts of atmospheric importance. *Atmos. Environ.* 35 (7):1183–92. doi:10.1016/S1352-2310(00)00426-X.

Peng, L., Z. R. Li, G. H. Zhang, X. H. Bi, W. W. Hu, M. J. Tang, X. M. Wang, P. Peng, and G. Y. Sheng. 2021. A review of measurement techniques for aerosol effective density. *Sci. Total Environ.* 778:146248. doi:10.1016/j.scitotenv.2021.146248.

Perraud, V., X. X. Li, J. K. Jiang, B. J. Finlayson-Pitts, and J. N. Smith. 2020. Size-resolved chemical composition of sub-20 nm particles from methanesulfonic acid reactions with methylamine and ammonia. *ACS Earth Space Chem.* 4 (7):1182–94. doi:10.1021/acsearthspacechem.0c00120.

Phinney, L., W. R. Leaitch, U. Lohmann, H. Boudries, D. R. Worsnop, J. T. Jayne, D. Toom-Sauntry, M. Wadleigh, S. Sharma, and N. Shantz. 2006. Characterization of the aerosol over the sub-arctic north east Pacific Ocean. *Deep-Sea Res. Pt Ii* 53 (20-22):2410–33. doi:10.1016/j.dsr2.2006.05.044.

Pitz, M., O. Schmid, J. Heinrich, W. Birmili, J. Maguhn, R. Zimmermann, H.-R. Wichmann, A. Peters, and J. Cyrys. 2008. Seasonal and diurnal variation of PM2.5 apparent particle density in urvan air in Augsburg, Germany. *Environ. Sci. Technol.* 42 (14):5087–93. doi:10.1021/es7028735.

Pope, C. A., and D. W. Dockery. 2006. Health effects of fine particulate air pollution: Lines that connect. *J. Air Waste Manag. Assoc.* 56 (6):709–42. doi:10.1080/10473289.2006.10464545.

Pratt, K. A., and K. A. Prather. 2012. Mass spectrometry of atmospheric aerosols - Recent developments and applications. Part II: On-line mass spectrometry techniques. *Mass Spectrom. Rev.* 31 (1):17–48. doi:10.1002/mas.20330.

Qiu, C., and R. Y. Zhang. 2012. Physiochemical properties of alkylaminium sulfates: hygroscopicity, thermostability, and density. *Environ. Sci. Technol.* 46 (8):4474–80. doi:10.1021/es3004377.

Rissler, J., E. Z. Nordin, A. C. Eriksson, P. T. Nilsson, M. Frosch, M. K. Sporre, A. Wierzbicka, B. Svenningsson, J. Londahl, M. E. Messing, et al. 2014. Effective density and mixing state of aerosol particles in a near-traffic urban environment. *Environ. Sci. Technol.* 48 (11):6300–8. doi:10.1021/es5000353.

Ristimaki, J., A. Virtanen, M. Marjamaki, A. Rostedt, and J. Keskinen. 2002. On-line measurement of size distribution and effective density of submicron aerosol particles. *J. Aerosol Sci.* 33 (11):1541–57. doi:10.1016/S0021-8502(02)00106-4.

Rumble, J. R. 2022. *CRC handbook of chemistry and physics*. 103rd ed. *(Internet Version 2022)*. Boca Raton, FL: CRC Press/Taylor & Francis.

Sang, S. W., C. Chu, T. C. Zhang, H. Chen, and X. R. Yang. 2022. The global burden of disease attributable to ambient fine particulate matter in 204 countries and territories, 1990-2019: A systematic analysis of the Global Burden of Disease Study 2019. *Ecotoxicol. Environ. Saf.* 238:113588. doi:10.1016/j.ecoenv.2022.113588.

Schmale, J., J. Schneider, E. Nemitz, Y. S. Tang, U. Dragosits, T. D. Blackall, P. N. Trathan, G. J. Phillips, M. Sutton, and C. F. Braban. 2013. Sub-Antarctic marine aerosol: dominant contributions from biogenic sources. *Atmos. Chem. Phys.* 13 (17):8669–94. 105194/acp-13-8669-2013 doi:10.5194/acp-13-8669-2013.

Scientific Instrument Services (SIS). Compound summary for Santovac(R) 5 ultra vacuum pump fluid. https://www.sisweb.com/vacuum/sis/satovc5.htm, last viewed on Nov. 25, 2022.

Shen, W. C., L. L. Ren, Y. Zhao, L. Y. Zhou, L. Dai, X. L. Ge, S. F. Kong, Q. Yan, H. H. Xu, Y. J. Jiang, et al. 2017. C_1-C_2 alkyl aminiums in urban aerosols: Insights from ambient and fuel combustion emission measurements in the Yangtze River Delta region of China. *Environ. Pollut.* 230:12–21. doi:10.1016/j.envpol.2017.06.034.

Singh, A., W. J. Bloss, and F. D. Pope. 2017. 60 years of UK visibility measurements: impact of meteorology and atmospheric pollutants on visibility. *Atmos. Chem. Phys.* 17 (3):2085–101. doi:10.5194/acp-17-2085-2017.

Sipkens, T. A., U. Trivanovic, A. Naseri, O. W. Bello, A. Baldelli, M. Kazemimanesh, A. K. Bertram, L. Kostiuk, J. C. Corbin, J. S. Olfert, et al. 2021. Using two-dimensional distributions to inform the mixing state of soot and salt particles produced in gas flares. *J. Aerosol Sci.* 158:105826. doi:10.1016/j.jaerosci.2021.105826.

Smith, J. N., K. C. Barsanti, H. R. Friedli, M. Ehn, M. Kulmala, D. R. Collins, J. H. Scheckman, B. J. Williams, and P. H. McMurry. 2010. Observations of aminium salts in atmospheric nanoparticles and possible climatic implications. *Proc. Natl. Acad. Sci. U S A* 107 (15):6634–9. doi:10.1073/pnas.0912127107.

Smith, J. N., D. C. Draper, S. Chee, M. Dam, H. Glicker, D. Myers, A. E. Thomas, M. J. Lawler, and N. Myllys. 2021. Atmospheric clusters to nanoparticles: Recent progress and challenges in closing the gap in chemical composition. *J. Aerosol Sci.* 153:105733. doi:10.1016/j.jaerosci.2020.105733.

Song, Y., X. Y. Pei, H. C. Liu, J. J. Zhou, and Z. B. Wang. 2022. Characterization of tandem aerosol classifiers for selecting particles: Implication for eliminating the

multiple charging effect. *Atmos. Meas. Tech.* 15 (11): 3513–26. doi:10.5194/amt-15-3513-2022.

Stein, S. W., B. J. Turpin, X. P. Cai, C. P. F. Huang, and P. H. Mcmurry. 1994. Measurements of relative humidity-dependent bounce and density for atmospheric particles using the DMA-impactor technique. *Atmos. Environ.* 28 (10):1739–46. Doi doi:10.1016/1352-2310(94)90136-8.

Sullivan, A. P., K. B. Benedict, C. M. Carrico, M. K. Dubey, B. A. Schichtel, and J. C. Collett. 2020. A quantitative method to measure and speciate amines in ambient aerosol samples. *Atmosphere-Basel* 11 (8):808. ARTN 808, doi: 10.3390/atmos11080808.

Symonds, J. P. R., K. S. Reavell, and J. S. Olfert. 2013. The CPMA-electrometer system - A suspended particle mass concentration standard. *Aerosol Sci Tech* 47 (8):I–Iv. doi: 10.1080/02786826.2013.801547.

Tajima, N., H. Sakurai, N. Fukushima, and K. Ehara. 2013. Design considerations and performance evaluation of a compact aerosol particle mass analyzer. *Aerosol Sci. Tech.* 47 (10):1152–62. doi:10.1080/02786826.2013.827323.

Tang, M. J., L. Y. Guo, Y. Bai, R. J. Huang, Z. Wu, Z. Wang, G. H. Zhang, X. Ding, M. Hu, and X. M. Wang. 2019. Impacts of methanesulfonate on the cloud condensation nucleation activity of sea salt aerosol. *Atmos. Environ.* 201:13–7. doi:10.1016/j.atmosenv.2018.12.034.

Tavakoli, F., and J. S. Olfert. 2014. Determination of particle mass, effective density, mass-mobility exponent, and dynamic shape factor using an aerodynamic aerosol classifier and a differential mobility analyzer in tandem. *J. Aerosol Sci.* 75:35–42. doi:10.1016/j.jaerosci.2014.04.010.

Titosky, J., A. Momenimovahed, J. C. Corbin, K. Thomson, G. Smallwood, and J. S. Olfert. 2019. Repeatability and intermediate precision of a mass concentration calibration system. *Aerosol Sci. Tech.* 53 (6):701–11. doi:10.1080/02786826.2019.1592103.

VWR. https://ie.vwr.com/store/product/7193525/1-4-diaminobutane-dihydrochloride-sigma-aldrich.

Wang, S., S. Crumeyrolle, W. Zhao, X. Xu, B. Fang, Y. Derimian, C. R. Chen, W. Chen, W. Zhang, Y. Huang, et al. 2021. Real-time retrieval of aerosol chemical composition using effective density and the imaginary part of complex refractive index. *Atmos. Environ.* 245:117959. doi:10.1016/j.atmosenv.2020.117959.

Wang, Z., S. M. King, E. Freney, T. Rosenoern, M. L. Smith, Q. Chen, M. Kuwata, E. R. Lewis, U. Poschl, W. Wang, et al. 2010. The dynamic shape factor of sodium chloride nanoparticles as regulated by drying rate. *Aerosol Sci. Tech.* 44 (11):939–53. doi:10.1080/02786826.2010.503204.

Wingen, L. M., and B. J. Finlayson-Pitts. 2019. Probing surfaces of atmospherically relevant organic particles by Easy Ambient Sonic-Spray Ionization Mass Spectrometry (EASI-MS). *Chem. Sci.* 10 (3):884–97. doi:10.1039/c8sc03851a.

Xu, W., J. Ovadnevaite, K. N. Fossum, C. Lin, R.-J. Huang, C. O'Dowd, and D. Ceburnis. 2020. Aerosol hygroscopicity and its link to chemical composition in the coastal atmosphere of Mace Head: Marine and continental air masses. *Atmos. Chem. Phys.* 20 (6):3777–91. doi:10.5194/acp-20-3777-2020.

Yao, Q., A. Asa-Awuku, C. D. Zangmeister, and J. G. Radney. 2020. Comparison of three essential submicrometer aerosol measurements: Mass, size and shape. *Aerosol Sci. Tech.* 54 (10):1197–209. doi:10.1080/02786826.2020.1763248.

Zelenyuk, A., Y. Cai, L. Chieffo, and D. Imre. 2005. High precision density measurements of single particles: The density of metastable phases. *Aerosol Sci. Tech.* 39 (10): 972–86. doi:10.1080/02786820500380206.

Zelenyuk, A., Y. Cai, and D. Imre. 2006. From agglomerates of spheres to irregularly shaped particles: Determination of dynamic shape factors from measurements of mobility and vacuum aerodynamic diameters. *Aerosol Sci. Tech.* 40 (3):197–217. doi:10.1080/02786820500529406.

Zhou, S. Q., J. Lin, X. F. Qin, Y. Chen, and C. R. Deng. 2018. Determination of atmospheric alkylamines by ion chromatography using 18-crown-6 as mobile phase additive. *J. Chromatogr. A.* 1563:154–61. doi:10.1016/j.chroma.2018.05.074.

Zhou, Y. Q., N. Ma, Q. Q. Wang, Z. B. Wang, C. R. Chen, J. C. Tao, J. Hong, L. Peng, Y. He, L. H. Xie, et al. 2022. Bimodal distribution of size-resolved particle effective density: Results from a short campaign in a rural environment over the North China Plain. *Atmos. Chem. Phys.* 22 (3):2029–47. doi:10.5194/acp-22-2029-2022.